Mapping Orientational Order in a Bulk Heterojunction Solar Cell with Polarization-Dependent Photoconductive Atomic Force Microscopy

Christopher J. Takacs,[†,§] Samuel D. Collins,[‡,§] John A. Love,[‡] Alexander A. Mikhailovsky,[‡] David Wynands,[‡] Guillermo C. Bazan,[∞,‡] Thuc-Quyen Nguyen,[∞,‡,¥,*] and Alan J. Heeger[†,*]

[†]Department of Physics, [∞]Department of Chemistry and Biochemistry and [‡]Center for Polymers and Organic Solids, University of California Santa Barbara, Santa Barbara, California 93106, United States, and [¥]Department of Chemistry, Faculty of Science, King Abdulaziz University, Jeddah, Saudi Arabia. [§]C. J. Takacs and S. D. Collins contributed equally.

ABSTRACT New methods connecting molecular structure, self-organization, and optoelectronic performance are important for understanding the current generation of organic photovoltaic (OPV) materials. In high power conversion efficiency (PCE) OPVs, light-harvesting small-molecules or polymers are typically blended with fullerene derivatives and deposited in thin films, forming a bulk heterojunction (BHJ), a self-assembled three-dimensional nanostructure of electron donors and acceptors that separates and transports charges. Recent data suggest micrometer-scale orientational order of donor domains exists within this complex nanomorphology, but the link to the optoelectronic properties is yet unexplored. Here we introduce polarization-dependent, photoconductive atomic force microscopy (pd-pcAFM) as a combined probe of orientational order and nanoscale optoelectronic properties (~20 nm resolution). Using the donor 7,7′-(4,4-bis(2-ethylhexyl)-4*H*-silolo[3,2-*b*:4,5-*b*′]dithiophene-2,6-diyl)bis(6-fluoro-4-(5′-hexyl[2,2′-bithiophen]-5-yl)benzo[*c*][1,2,5]thiadiazole), p-DTS(FBTTh$_2$)$_2$, we show significant spatial dependence of the nanoscale photocurrent with polarized light in both pristine and BHJ blends (up to 7.0% PCE) due to the local alignment of the molecular transition dipoles. By mapping the polarization dependence of the nanoscale photocurrent, we estimate the molecular orientation and orientational order parameter. Liquid crystalline disclinations are observed in all films, in agreement with complementary electron microscopy experiments, and the order parameter exceeds 0.3. The results demonstrate the utility of pd-pcAFM to investigate the optical/structural anisotropy that exists within a well-performing BHJ system and its relationship to optoelectronic properties on both the nanometer and micrometer length scales.

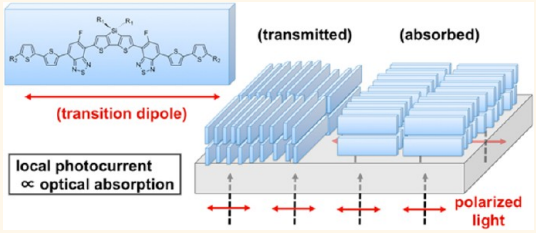

KEYWORDS: bulk heterojunction · long-range order · liquid crystal · photoconductive atomic force microscopy · conjugated small molecule · organic photovoltaics

Both research and commercial interest in organic photovoltaics (OPVs) continue to increase as power conversion efficiencies (PCEs) exceed 10%.[1] The best of these devices are based on the bulk heterojunction (BHJ) concept, where electron donors and acceptors self-assemble in three dimensions. Ideally, photoexcitations are within ~20 nm of a donor/acceptor heterojunction and undergo charge separation. Once separated, a built-in field drives the electron (hole) through continuous pathways of acceptor (donor) molecules over a distance on the order of 100 nm to be collected at the cathode (anode). The self-organization of the solid thin film plays a critical role in the optoelectronic function of these devices. Consequently, great effort has been made to optimize morphology through improved purity, changes in molecular structure, and processing of the blend films.[2]

Recently, solution-processable, small-molecule donor materials such as 7,7′-(4,4-bis(2-ethylhexyl)-4*H*-silolo[3,2-*b*:4,5-*b*′]dithiophene-2,6-diyl)bis(6-fluoro-4-(5′-hexyl[2,2′-bithiophen]-5-yl)benzo[*c*][1,2,5]-thiadiazole), p-DTS(FBTTh$_2$)$_2$ (Figure 1a), have become an attractive alternative to polymer donor materials due to their facile synthesis, high purity, and competitive PCE.[3−12] Using the electron acceptor [6,6]-phenyl-C$_{70}$-butyric acid methyl ester (PC$_{70}$BM) and

* Address correspondence to quyen@chem.ucsb.edu; ajhe1@physics.ucsb.edu.

Received for review April 25, 2014 and accepted July 14, 2014.

Published online July 31, 2014
10.1021/nn502277d

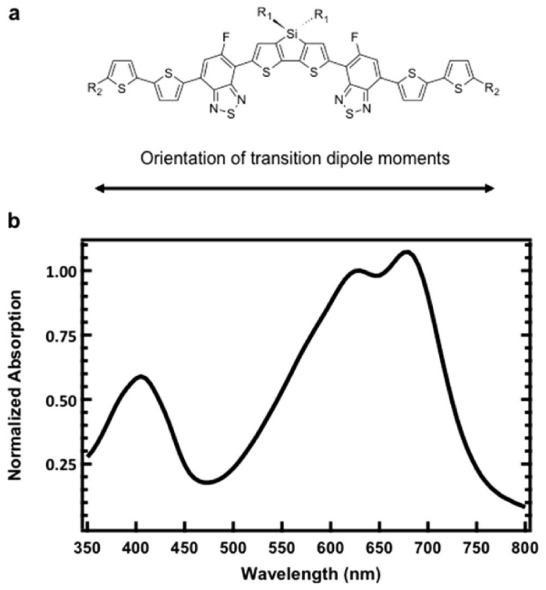

Figure 1. (a) Molecular structure of p-DTS(FBTTh$_2$)$_2$. R_1 = 2-ethylhexyl; R_2 = *n*-hexyl. (b) Thin-film absorption spectrum of p-DTS(FBTTh$_2$)$_2$. Gas-phase, single-molecule density functional theory calculations (Table S1) show the transition dipole moments are parallel to the molecular long axis for the conformation in part (a).

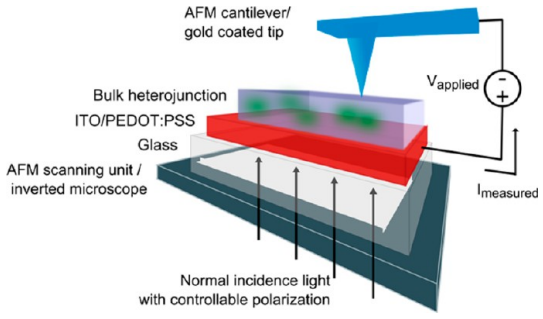

Figure 2. Schematic of polarization-dependent photoconductive AFM. The p-DTS(FBTTh$_2$)$_2$:PC$_{70}$BM BHJ sample is mounted atop an inverted microscope with the illumination through the glass/ITO/PEDOT:PSS layers. The gold-coated AFM tip is brought into contact with the BHJ layer to act as the back electrode. A small bias is applied between the tip and ITO electrode, and the photocurrent is measured while scanning the tip across the sample. The wavelength and incident polarization vector, which lies in the sample plane, are computer controlled.

appropriate processing conditions, the PCE can exceed 7%. Previous studies have shown that processing can strongly alter donor crystallinity and crystallite size, influencing the optoelectronic performance, but much still remains to understand about these well-performing systems. Interestingly, in addition to the small donor crystallites, structural studies demonstrate the existence of in-plane ordering on a second length scale in p-DTS(FBTTh$_2$)$_2$ (*vide infra*) and similar, isomorphic derivatives: a micrometer-scale orientational order of donor material.[13] This orientational order exists not only in the pure donor films but also in BHJ blends as part of the nanostructured donor/acceptor network. The connection of this micrometer-scale order to the optoelectronic function has yet to be explored and represents an intriguing aspect of these well-performing materials.[13,14]

Here we investigate the connection of long-range order and the optoelectronic properties using a new technique: polarization-dependent, photoconductive atomic force microscopy (pd-pcAFM). The pd-pcAFM method combines the well-established pcAFM technique,[15−19] a probe of nanoscale photocurrent and electronic transport, with the polarization-dependent optical absorption of most organic molecules to investigate local orientational order. In traditional pcAFM, a small bias is applied between a conductive AFM probe and a planar bottom electrode while illuminating the sample *via* an inverted optical microscope (Figure 2). Photons absorbed throughout the active layer can lead to photogenerated free carriers, which are transported through the three-dimensional morphology and collected by the tip. The bias is chosen to selectively collect photogenerated electrons *or* holes, and it is small to ensure minimal injection of carriers into the active layer.[16] Photocurrent is then mapped out over the active layer surface at high spatial resolution (∼20 nm), enabling detailed study of nanoscale optoelectronic properties under a variety of operating conditions and elucidating the link between nanoscale electronic properties and macroscopic device performance. The pd-pcAFM method adds a new dimension to pcAFM data acquisition and interpretation. Monochromatic, polarized light with a controllable in-plane polarization direction is used to illuminate the sample at normal incidence. The light polarization introduces molecular orientation dependence into the photon absorption and charge-generation rate; multiple photocurrent maps of the same sample area are then acquired for different polarization directions. The polarization dependence of the local photocurrent reflects the degree of nanoscale orientational order and provides a link between morphology and optoelectronic properties at a spatial resolution beyond the diffraction limit of an optical microscope.

Polarized photocurrent images were collected from p-DTS(FBTTh$_2$)$_2$ BHJ films as well as from pure donor film. We show that polarization-dependent, micrometer-scale charge generation exists in all samples as a consequence of the local alignment of the transition dipoles. Maps of the orientational order are in qualitative agreement with complementary dark-field transmission electron microscopy (TEM) experiments and suggest that a liquid crystalline order of the donor material exists within all thin films. From analysis of pd-pcAFM data, a lower bound on the average nanoscale order parameter is estimated to be ∼0.3, suggesting a large degree of local alignment. These results demonstrate the utility of pd-pcAFM in probing anisotropy in the optoelectronic properties and morphology.

TABLE 1. Solar Cell Device Parameters as a Function of Solvent Additive Concentration and Fullerene Derivative.

v/v % DIO	acceptor	J_{sc} [mA cm^{-2}]	fill factor [%]	V_{oc} [mV]	PCE
0.4%[a]	$PC_{70}BM$	12.8	68	809	7.0
0%[a]	$PC_{70}BM$	6.6	36	780	1.8
0.4%	$PC_{60}BM$	10.46	67	803	5.7

[a] Device parameters reproduced from ref 3.

RESULTS AND DISCUSSION

Optical Absorption. The thin-film absorption spectrum of pristine p-DTS(FBTTh$_2$)$_2$ shows two major absorption bands around 410 and 670 nm characteristic of the intramolecular donor−acceptor interactions as well as a vibronic replica (~620 nm), consistent with aggregation in the solid state (Figure 1b). Following the time-dependent density functional theory calculations of Zhugayevych *et al.*,[20] the orientation and amplitude of the transition dipole moments of a single molecule were calculated at the CAM-B3LYP/6-31G* level of theory in the conformation previously observed in the single-crystal structure (Figure 1a). The calculated transition dipole moments within the low- and high-energy bands lie along the molecular long axis. For other low-lying molecular conformations likely present in the thin film, the low-energy transition dipoles likely remain near the molecular long axis; however, the orientation of the higher energy transitions may change (Supporting Information). Detailed spectroscopic analysis of similar materials found the intermolecular interactions are relatively weak;[21] thus, approximating the transition dipole moment of the crystal along the molecular long axes is expected to be sufficient for the purposes of this study. Light absorption is expected to follow the usual $\cos^2(\theta)$ dependence for θ, the angle between the incident polarization vector and the transition dipole.

Since the purpose of the study reported herein is to elucidate the connection between the nanoscale optoelectronic properties and morphology in BHJ films, [6,6]-phenyl-C$_{61}$-butyric acid methyl ester ($PC_{60}BM$) was substituted for $PC_{70}BM$ to suppress absorption from the fullerene where necessary but with no loss in generality (Table 1).

Thin-Film Morphology. To put the development of the pd-pcAFM technique in the proper context and preface the peculiar optoelectronic properties, TEM is used to establish the coexistence of a complex nanostructure and long-range orientational order within the optimized blend film. Figure 3a shows a typical high-resolution TEM (HRTEM) image of a p-DTS(FBTTh$_2$)$_2$:$PC_{60}BM$ blend film with 0.4% v/v 1,8-diiodooctane (DIO) as a cosolvent. These processing conditions have been found empirically to yield the best PCE (Table 1).[4] TEM gives a projection of the structure through the full thickness of the film (~80 nm) and has been used to great effect to understand the ordering in organic systems.[22−26] The lattice planes of the donor crystallites, corresponding to alkyl stacking, with a *d*-spacing of 2.2 nm, are the most obvious feature under these imaging conditions, although it should also be understood that only fibers satisfying the Bragg condition are visible. Previous studies show that these fibers extend throughout the thickness of the film, bending and twisting in three dimensions.[27] While the relative orientations of nearby fibers are likely partially correlated, many directions are still observed locally. The nominal width of the fibers in this "rice-grain" structure is 10−20 nm,[27] length scales commonly believed to best balance charge generation and charge transport in small-molecule and polymer active layers.[2,3,28]

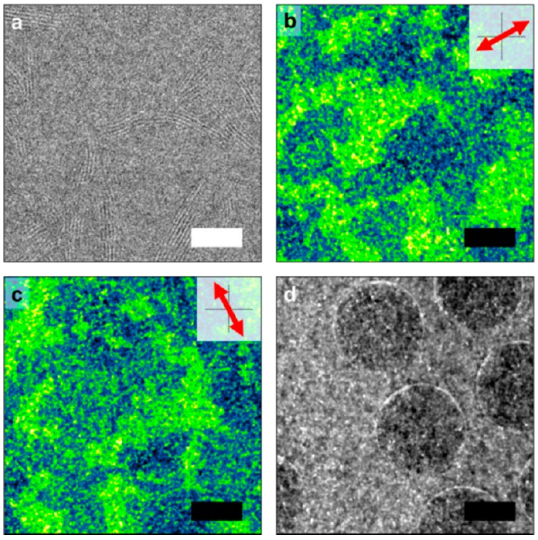

Figure 3. (a) HRTEM image showing lattice planes, *d*-spacing of 2.2 nm, of fiber-like structures in a p-DTS(FBTTh$_2$)$_2$:$PC_{60}BM$ film processed with 0.4% v/v DIO. (b, c) Dark-field images of orthogonal crystallite directions at a fixed location. The image intensity, in order of increased scattering, goes black, blue, green, yellow, white. Micrometer-scale order is visible along with smaller, randomly oriented crystallites. (d) Sum of the 12 dark-field images covering all in-plane directions at the same location. Only the 2 μm holes of the TEM grid are visible, suggesting the micrometer-scale order covers the film. The white (black) scale bar is 30 nm (1.2 μm).

The situation is quite different for crystallites of the donor molecule that $\pi-\pi$ stack in-plane (*d*-spacing of ~3.6 Å); dark-field TEM can be used to image the micrometer-scale orientational order of this crystal population.[13,26] In a single dark-field TEM image, bright regions denote crystalline regions with an in-plane orientation. This orientation is determined by the position of a small aperture in the back focal plane of the objective lens and can be easily controlled to probe any in-plane orientation. Twelve total dark-field images at a fixed location were taken to cover all in-plane crystallite orientations. Two images with orthogonal crystallite directions are shown in Figure 3b and c, respectively. Both show micrometer-scale structures

consistent with agglomerates of smaller crystallites in similar orientations, along with speckles resulting from quasi-randomly oriented crystallites. The two images are nearly complementary; that is, bright regions in Figure 3b, denoting crystallites oriented in a particular direction, correlate well with dark regions in Figure 3c, signifying an absence of crystallites oriented in a perpendicular direction. In total, the micrometer-scale locally oriented features cover the blend film as evidenced by the uniformity of the summed images (Figure 3d) and an animation of the azimuthal dark-field image series showing the smooth deformations in the local crystal orientation (Supporting Information). Thus, the donor self-organizes on both nanometer and micrometer length scales in a well-performing device.

For reference, the BHJ processed without the solvent additive shows no fiber-like texture in the HRTEM images, and no indication of significant phase separation is observed, consistent with the lower device performance (Table 1).[27] Interestingly, this film also shows long-range order of the in-plane $\pi-\pi$ stacking population of similar length scale to the optimized BHJ (Figure S6).

The diffraction and order of the pristine donor film are exceptional compared to either of the BHJ blends, and the length scale of the long-range order is increased. Dark-field images of orthogonal crystallite orientations with complementary coverage are presented in Figure 4. These images suggest orientational order over several micrometers, and the sum of the azimuthal dark-field image series (Figure 4c) is uniform except for a few dark regions. These dark regions are likely also crystalline, but may be either slightly misoriented such that the Bragg condition is no longer satisfied or in a different orientation. HRTEM images show large crystals with a *d*-spacing of 2.2 nm, although they are relatively rare and cover a small fraction of the film. An example of such a crystal is shown in Figure 4. The results indicate that while the fullerene and solvent additives strongly modify the self-assembly process within these blends, long-range order is intrinsic to the donor material.

pd-pcAFM. The common local orientation of the donor molecules implies alignment of their transition dipoles and locally anisotropic optical properties. It follows that the local optical absorption and charge generation depend on the incident light polarization in a manner reflective of the underlying molecular orientation and local morphology. To simultaneously measure the polarization dependence of the nanoscale photocurrent and minimize drift during pd-pcAFM acquisition, scanning is interleaved in the $+y$ direction with a combination of four in-plane polarization directions and/or wavelengths. After deinterleaving, the pixel resolution of each photocurrent map is 512 px × 128 px with a physical aspect ratio of 1:1. A positive bias ranging between 0.5 and 1.5 V was applied to the substrate such that the gold-coated tip selectively probes the local photogenerated hole current, making it most sensitive to the donor material. The contribution of charge injection (*i.e.*, the dark current) is small compared to the photocurrent contrast. In effect, the nanoscale device is analogous to a photodetector, and the response depends on local charge generation and charge collection. Fortunately, the charge-generation rate is expected to be proportional to the optical absorption and the charge collection is approximately independent of the illumination conditions; thus, *relative* changes in the polarization-dependent photocurrent reflect the local molecular orientation at each point on the sample.

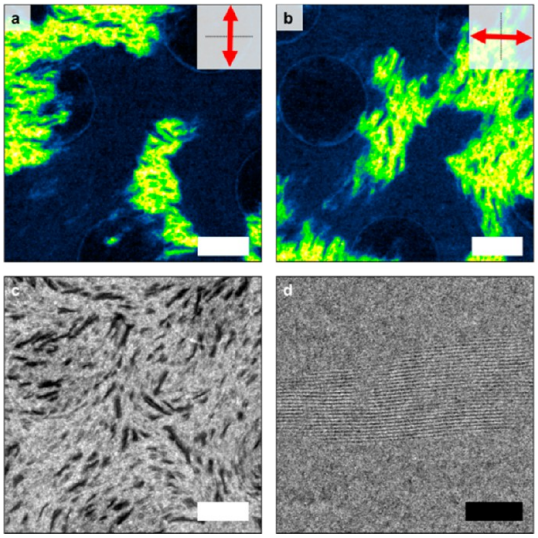

Figure 4. (a, b) Dark-field images of pure p-DTS(FBTTh$_2$)$_2$ films with orthogonal orientations. Red arrows show the approximate in-plane crystallite orientation. (c) Sum of the 12 dark-field images that cover all possible in-plane crystallite orientations. (d) HRTEM image showing a portion of a large crystallite with a *d*-spacing of 2.2 nm. Such crystals are relatively rare. The white (black) scale bar is 1.2 μm (35 nm).

The p-DTS(FBTTh$_2$)$_2$:PC$_{60}$BM BHJ films processed with and without the solvent additive show micrometer-scale photocurrent anisotropy for both polarized 650 and 405 nm wavelengths (Figure 5 and Figure 6). Along a fixed polarization direction, both wavelengths give rise to near identical micrometer-scale structure, consistent with the transition dipoles being collinear with the molecular long-axis and oriented in-plane. Significant changes in the photocurrent are also observed after rotating the in-plane polarization by 90°. This strongly indicates that the large-scale changes in the photocurrent are not the result of dead regions within the device. If the local polarization-dependent optical absorption of the thin film is proportional to $\cos^2(\theta)$, an approximation that neglects self-absorption through the film thickness, optical interference effects, and any nonidealities in the photocurrent collection process, the sum of any orthogonal pair of photocurrent maps is complementary

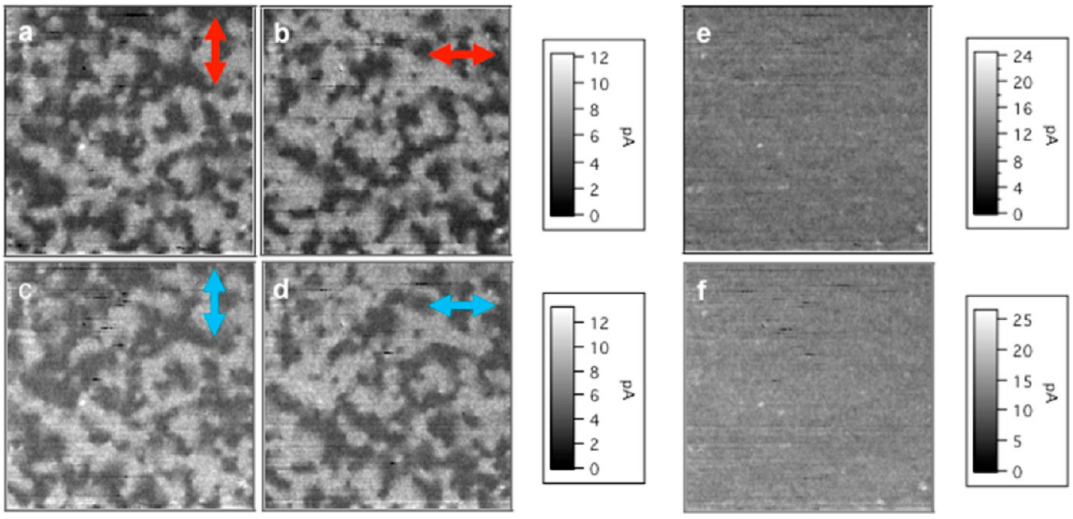

Figure 5. Two pairs of orthogonal, polarized photocurrent maps for incident 650 nm (a and b) and 405 nm (c and d) light all taken from the same location of a p-DTS(FBTTh$_2$)$_2$:PC$_{60}$BM BHJ film processed without the solvent additive. Both wavelengths show nearly identical, micrometer-scale anisotropy and complementary structure for the orthogonal polarization. The incident polarization direction and wavelength are indicated in the upper right of each image. The sum of the two orthogonal photocurrent maps at 650 nm (e) and 405 nm (f) are almost completely uniform. All images are 10 μm $\times$ 10 μm in size.

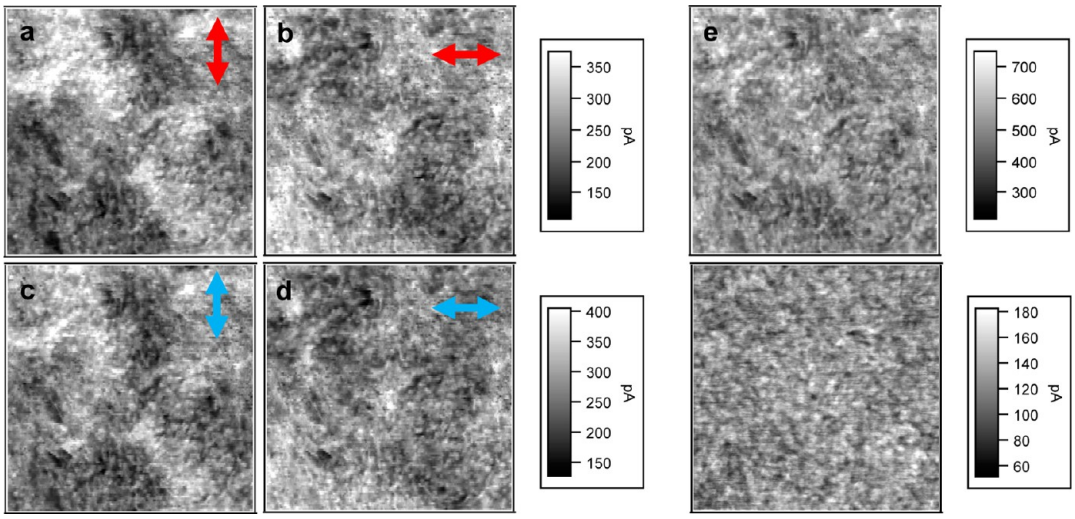

Figure 6. Two pairs of orthogonal, polarized photocurrent maps for incident (a, b) 650 nm and (c, d) 405 nm light, all taken from the same location of a p-DTS(FBTTh$_2$)$_2$:PC$_{60}$BM BHJ film with 0.4% v/v DIO. Both wavelengths show nearly identical, micrometer-scale anisotropy and complementary structure for the orthogonal polarization. The incident polarization direction and wavelength are indicated in the upper right of each image. The sum of the two orthogonal photocurrent maps at 650 nm (e) is more uniform, similar to focused white light (f) taken at another location on the sample. All images are 5 μm $\times$ 5 μm in size.

and the result is similar to the "polarization-averaged" or unpolarized photocurrent response, *i.e.*, $\cos^2(\theta) + \cos^2(\theta + 90°) = 1$. For the BHJ film processed without the additive, the sums of the 650 and 405 nm orthogonal photocurrent maps are shown in Figure 5e and f, respectively. Both summed images are nearly uniform on the micrometer scale, implying the polarization-averaged photoresponse is remarkably homogeneous despite the large-scale structural heterogeneity. For the optimized BHJ, micrometer-scale structure is also visible in the polarized photocurrent maps in addition to nanoscale features that are presumably fluctuations in the local hole mobility related to donor−acceptor phase separation and the well-developed fiber morphology observed with TEM. Much of the large-scale structure is complementary. The sum of the orthogonal maps (Figure 6e) is more uniform than either individual photocurrent map, but the sum shows some residual large-scale inhomogeneity (Figure 6e) not present in photocurrent maps taken with unpolarized, highly focused white-light illumination (Figure 6f). This residual inhomogeneity is believed to be linked to the exponential absorption through the film thickness, which leads to small distortions from the expected $\cos^2(\theta)$ profile (Supporting Information). Remarkably, the length scales observed in the raw pd-pcAFM and

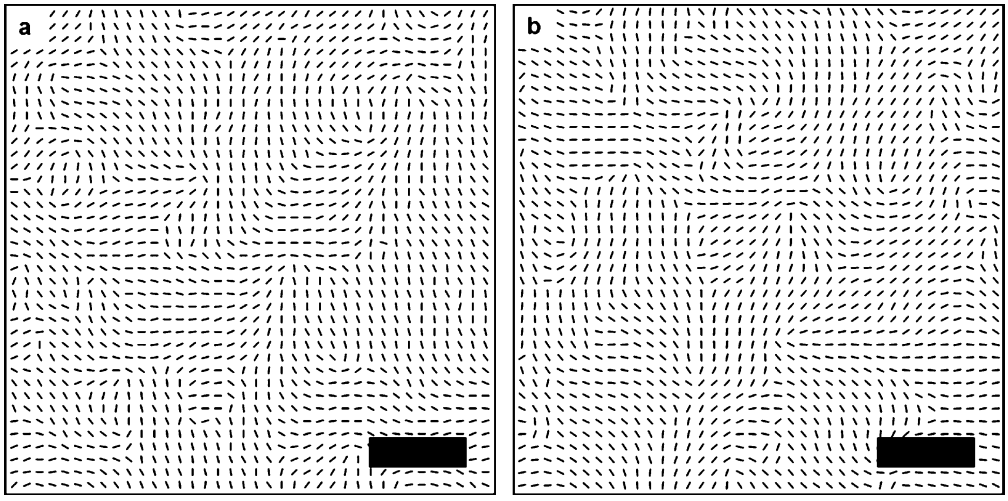

Figure 7. Director field constructed from (a) pd-pcAFM and (b) dark-field TEM images of a p-DTS(FBTTh$_2$)$_2$:PC$_{70}$BM BHJ film with 0.4% v/v DIO. The data are taken from separate but identically prepared samples. Both methods give comparable, micrometer-scale structure, suggesting they probe the same internal order of the BHJ film. The scale bar is 1 μm.

dark-field TEM data qualitatively agree, but additional analysis will be required to directly compare the two techniques.

By assuming a simple model of the polarization-dependent photocurrent, the information from multiple photocurrent maps can be combined to estimate molecular orientation and the degree of orientational order at each point on the sample. Four photocurrent maps with in-plane polarization vectors of 0°, 45°, 90°, and 135° are fit to an isotropic background with a single dipole-like dependence as in eq 1:

$$I(x,y;\beta) = A(x,y) + 2B(x,y)\cos^2(\beta - \phi(x,y)) \quad (1)$$

where the in-plane polarization direction is β, $I(x,y;\beta)$ is the local photocurrent, $A(x,y)$ is the polarization-independent current, and $2B(x,y)\cos^2(\beta - \phi(x,y))$ is the polarization-dependent current contribution of molecules oriented at an angle $\phi(x,y)$. It is useful to equate $\phi(x,y)$ with the molecular director, which represents the average local orientation of the molecules at any point on the film. By assuming the photocurrent is proportional to the local absorbance, the local anisotropy can be used to define a lower bound on a two-dimensional orientational order parameter. The pointwise dichroic ratio, the ratio of the local absorbance parallel and perpendicular to the direction of molecular alignment, can be written as $R(x,y) = (A(x,y) + 2B(x,y))/A(x,y)$, the ratio between the nanoscale photocurrents parallel and perpendicular to the local molecular director. The orientational order parameter can then be defined as $S = \langle (R(x,y) - 1)/(R(x,y) + 1)\rangle_{(x,y)}$ where a lower (upper) bound of $S = 0$ ($S = 1$) indicates a completely isotropic (oriented) structure at each point on the film.[29] This order parameter represents the average nanoscale alignment expected at any point on the sample and is applicable for films that are isotropic on macroscopic length scales.

By estimating the molecular director, the pd-pcAFM and dark-field TEM data can be compared side-by-side for the p-DTS(FBTTh$_2$)$_2$:PC$_{70}$BM BHJ processed with 0.4% v/v DIO. The local molecular orientation determined by pd-pcAFM is shown in Figure 7a using a 630 nm excitation wavelength. The map is a visualization of $\phi(x,y)$ in the form of a director field, a grid of short lines drawn parallel to the proposed molecular long axis, and the micrometer-scale orientational order is clearly visible. It is worth noting that the film topography, which is acquired simultaneously with the pd-pcAFM data (Figure S2b), is relatively smooth and unremarkable in these BHJ samples with no clear indication of micrometer-scale orientational order. An equivalent analysis is performed for the dark-field image series (Supporting Information), and the result is shown in Figure 7b. The length scale and spatial structure from pd-pcAFM and dark-field TEM are qualitatively indistinguishable. This suggests the two radically different techniques likely probe a similar aspect of the internal order.

In all films investigated the director fields are reminiscent of a liquid crystalline state. Detailed examination of the director fields at higher resolution shows what appear to be $\pm 1/2$ disclinations in all samples. A comparison between the p-DTS(FBTTh$_2$)$_2$:PC$_{70}$BM BHJ film with 0.4% v/v DIO and p-DTS(FBTTh$_2$)$_2$:PC$_{60}$BM BHJ film without solvent additive is shown in Figure 8. The disclinations occur frequently, often observed in conjugate pairs, with the distance between disclination cores sometimes less than 500 nm. Despite the differences in crystallinity, phase separation, and device parameters, it seems the liquid crystalline nature associated with the π–π stacking of p-DTS(FBTTh$_2$)$_2$ within the blends is independent of additive.

For the pure film, along with the liquid crystalline structure, pinholes/defects in the film topography are

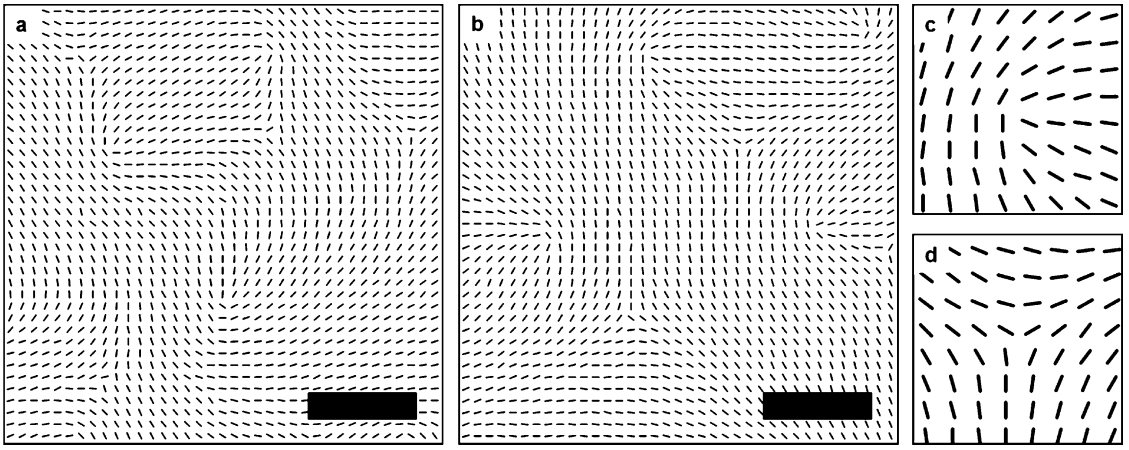

Figure 8. Reconstructed director field from high-resolution pd-pcAFM scans of (a) p-DTS(FBTTh$_2$)$_2$:PC$_{70}$BM BHJ with 0.4% v/v DIO and (b) p-DTS(FBTTh$_2$)$_2$:PC$_{60}$BM BHJ. Examples of +1/2 and −1/2 disclinations extracted from the p-DTS(FBTTh$_2$)$_2$:PC$_{60}$BM blend film are shown in part (c) and (d), respectively. The scale bars are 500 nm.

observed in the center of each imaged disclination. To demonstrate this correlation, the film topography is overlaid by the estimated molecular director $\phi(x,y)$ as shown in Figure 9. The molecular orientation is represented by both the short lines of the director field and a color-coded overlay of $\phi(x,y)$ to improve the effective resolution. As the topography is included primarily to show the pinholes/defects, the height is scaled from white (+5 nm) to black (−20 nm) with regions >20 nm below the film surface shown as solid blue. Some fine-grain structure is apparent in the topography, but the film is smooth compared to other studies of p-DTS-(FBTTh$_2$)$_2$, where long-range order is directly apparent.[30] During imaging, the pinholes/defects do change the contact with the AFM tip, which changes the photocurrent to some extent, but the polarization dependence of the photocurrent is still readily apparent (Supporting Information). From the pd-pcAFM data, the disclinations are clearly visible across the film. Remarkably, a pinhole/defect is observed at the center of each disclination, *i.e.*, a disclination core, and the depth tends to be >20 nm; however, not all surface defects/pinholes correspond to imaged disclinations. The formation of both the pinhole, a distortion of the film surface, and the disclination core, a line defect normal to film plane, is expected to cost energy. This observation of a pinhole/defect at the disclination core suggests that minimizing the length of the line defect by distorting the surface lowers the overall cost of the disclination.

The estimated lower bound for the orientational order parameter is approximately 0.3 in all films, which suggests a significant fraction of local alignment and a remarkable level of structural organization over length scales not typically considered in BHJ materials. The order parameter (photocurrent) exceeds 0.29 in the p-DTS(FBTTh$_2$)$_2$:PC$_{70}$BM BHJ device processed with 0.4% v/v DIO (∼170 pA at 2 V bias), 0.31 for the p-DTS(FBTTh$_2$)$_2$:PC$_{60}$BM BHJ device processed without DIO (∼10 pA at 1 to 1.5 V bias), and 0.31 for the pure p-DTS(FBTTh$_2$)$_2$ film (∼5 pA at 1.5 V bias). For all films, it is important to note that $R(x,y)$ shows some spatial dependence that appears correlated to surrounding features in the director field (Figure S11). $R(x,y)$ is highest in the well-aligned regions, with lower values in regions of higher bend/splay, which is consistent with a broader range of molecular orientations being present locally. In the BHJ films, it is interesting that the DIO, which is known to markedly change the time scale of the film formation process,[31] does not appear to significantly lower or raise the order parameter despite a nearly 10-fold increase in the photocurrent. We postulate that the liquid crystalline structure is a marker of an earlier lyotropic phase, and its formation is independent of the additive.

A better understanding of the role of long-range order in OPVs may lead to improved material design and device processing. Polarization-dependent photocurrents are likely observable in a variety of materials with both linear[26,32−34] and circularly polarized light.[35] Although most commonly discussed in the context of organic field-effect transistors,[34,36−41] orientational order may be beneficial for OPV devices, particularly for molecular semiconductors, which lack the intrinsic built-in connectivity of polymers. The local alignment may connect donor crystallites laterally through low-angle grain boundaries that provide alternative pathways to the anode.[13] Such effects could be important due to the highly anisotropic electronic properties of most organic crystals and the considerable effect grain boundaries are expected to have on charge-carrier transport. Alternatively, local orientational order can substantially reduce the absorption of unpolarized light (*e.g.*, sunlight) and lower the external quantum efficiency of optically thin or locally well-aligned devices, a concern particularly for directed morphologies (*e.g.*, lamellar block copolymers[42−45] and liquid crystalline materials[40,46]). In a single-layer OPV device that is

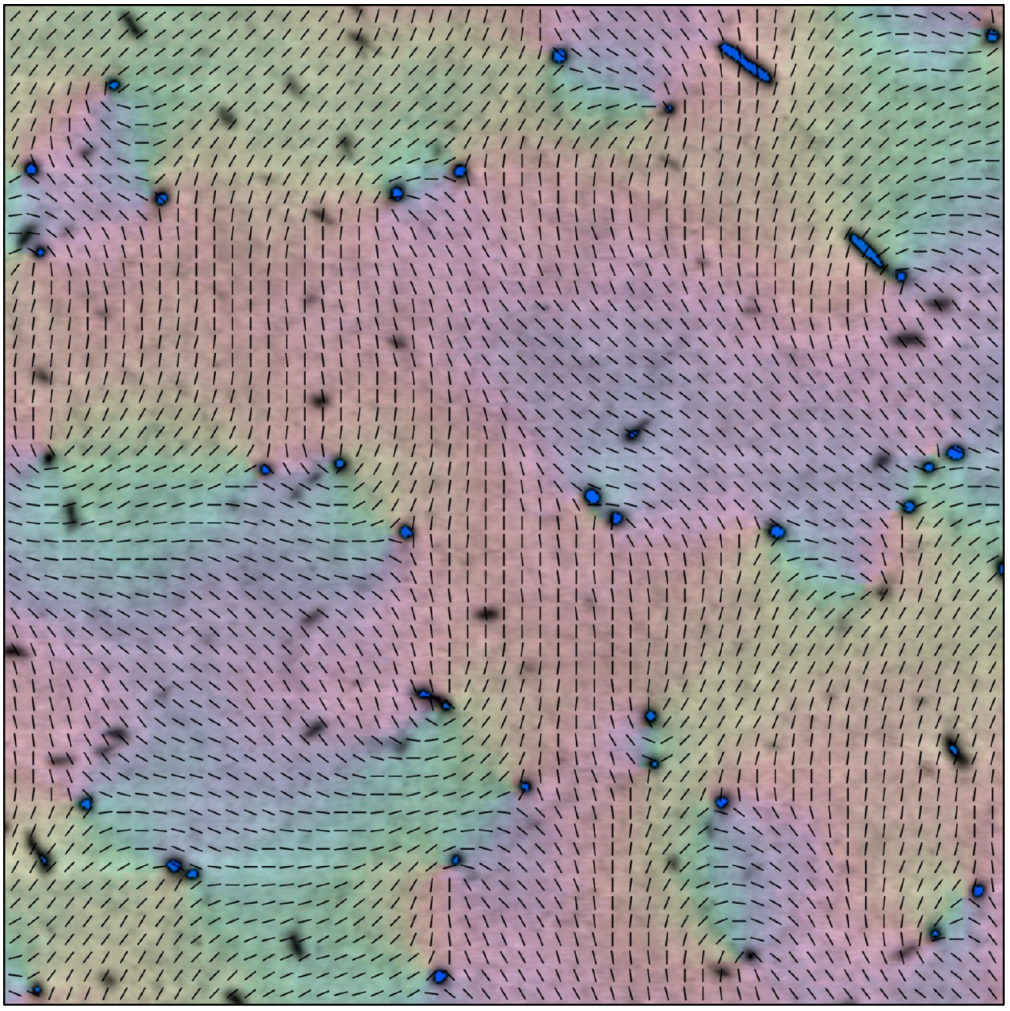

Figure 9. AFM topography of the pure p-DTS(FBTTh$_2$)$_2$ film overlaid by the director field. As the resolution of the director field is limited to the size of the lines, $\phi(x,y)$ is included as a color overlay to improve the resolution. The topography appears in gray scale from +5 nm to −20 nm with anything less than −20 nm displayed as solid blue. The image is 10 μm × 10 μm in size.

isotropic over macroscopic dimensions, the difference between polarized and unpolarized illumination is likely difficult to detect electronically; however, a subtle difference may be detectable in tandem devices, leading to an interesting class of polarization-sensitive photodetectors. In a tandem device, one layer can polarize the light for the next, which creates spatial fluctuations in charge-generation rates between layers that increase if the light is polarized. However, the lateral conductivity must be sufficiently low so that the local imbalances appreciably lower the overall PCE. The pd-pcAFM results also suggest that exploiting polarization-dependent sample interactions may be useful in other scanning probe techniques such as photopotential fluctuation spectroscopy,[47] electric force microscopy,[48,49] and scanning Kelvin probe microscopy to further probe the role of orientational order in organic semiconductors.[50]

As a technique, pd-pcAFM is complementary to other high-resolution probes of molecular organization such as TEM and soft X-ray scattering. With TEM, the existence of long-range order was inferred by local anisotropy in the $\pi-\pi$ scattering over micrometers, but the amplitude of the diffracted signal is not a reliable measure of local alignment. For example, the diffracted intensity visible in the dark-field image of the pure donor (Figure 4a,b) accounts for less than ~3% of the incident beam and ~0.3% in the BHJ films, making it challenging to balance electron beam damage and resolution.[24] In pd-pcAFM, the polarization dependence is easily related to the degree of local alignment, and the technique is not intrinsically destructive, leaving significant opportunities for further technique development, with important insights likely to follow. Soft X-ray characterization[32,33] also relies on the polarization-dependent absorption of high-energy transitions, corresponding to ionization of core-electrons to unoccupied molecular orbitals (~290 eV), from monochromatic synchrotron sources. These high-energy dipole transitions are normal to the plane of conjugation[33] (*i.e.*, in the direction of $\pi-\pi$ stacking) and *orthogonal* to the visible-light transition moments for

most conjugated molecules and polymers. This means pd-pcAFM probes orientational order in an orthogonal direction to STXM, allowing access to new aspects of the molecular organization.

CONCLUSIONS

The pd-pcAFM technique was developed as a general method combining polarization-dependent light–matter interactions with nanoscale charge generation and transport. Application to a high-performance BHJ device (7.0% PCE) revealed micrometer-scale, liquid crystalline order is integrated within the complex donor/acceptor BHJ structure in addition to a lower PCE device and the pristine donor material. It was demonstrated that the polarization dependence of the nanoscale photoconductivity can be used to reconstruct the local molecular orientation and estimate the orientational order parameter at high spatial resolution. By connecting the polarization-dependent optoelectronic properties with complementary TEM results, we demonstrated that the BHJ is not a random formation of "crystalline" and "amorphous" structures but an elegant and multifaceted manifestation of self-assembly over a broad range of length scales much larger than typically considered.

METHODS

Sample Fabrication. All active layers were spin-cast at 1750 rpm from 35 mg mL^{-1} of p-DTS($FBTTh_2$)$_2$:$PC_{60}BM$ or p-DTS($FBTTh_2$)$_2$:$PC_{70}BM$ (3:2 weight ratio) in chlorobenzene with 0.4% v/v 1,8-diiodoctane. Solutions were heated for several hours at 80 °C, and residual solids filtered before casting on PEDOT:PSS-coated glass/ITO substrates. After drying for 30 min, films processed with the solvent additive were heated to 70 °C for 10 min under a N_2 atmosphere. For solar cell devices, cathodes were deposited by sequential thermal evaporation of calcium (10 nm) and then aluminum (100 nm); the device properties were measured under 100 mW cm^{-2} simulated AM1.5G solar illumination.

TEM. TEM samples were prepared by delamination of the active layer in a DI water bath and transferred to a C-Flat TEM grid. Low-dose HRTEM images were acquired using SerialEM under approximately parallel illumination: the sample is translated and allowed to stabilize mechanically, the instrumental response is matched to the 2.2 nm *d*-spacing, the beam is blanked and shifted electronically to an undamaged region, and the image is acquired.[51] The HRTEM total electron dosage is 670 e^- nm^{-2}. Dark-field images were acquired using a 10 μm objective aperture (angular admittance of 55°) also using a low-dose procedure. The 12 dark-field images were acquired in pseudorandom order, covering the half azimuth with an angular resolution of 15° and an accumulated electron dose of 200 e^- nm^{-2}. The very low dose per image is to prevent electron damage from biasing the image series; an additional pair of dark-field images replicating the conditions of the first two is always acquired at the end of the series to check for electron damage effects. All images were taken on an FEI Titan operating at 300 kV.

pcAFM. The BHJ sample is deposited atop a glass/ITO/PEDOT:PSS electrode and mounted on an inverted optical microscope/AFM scanning stage. The inverted microscope illuminates the sample through the ITO/glass at normal incidence with a selectable 405, 633, or 650 nm polarized light. A gold-coated AFM probe acts as the back-electrode, and a small voltage is applied to collect photogenerated carriers. The photocurrent map is built by scanning the tip back and forth in the *x* direction, then incrementing the *y* direction and repeating until the full image is acquired.

All pcAFM images were collected using an Asylum MFP3D (Oxford Instruments) mounted above an Olympus inverted optical microscope located in an inert glovebox environment. Gold-coated silicon AFM tips with a resonant frequency of ~13 kHz and force constant of ~0.2 N m^{-1} (Budget Sensors) were used in all imaging. In unpolarized photoconductive measurements, a Xe lamp light source (Newport Oriel Instruments) was focused through the inverted optical microscope into a light spot approximately 150 μm in diameter. For polarized measurements of $PC_{60}BM$ samples, 650 and 405 nm laser diodes (Thorlabs CPS184 and CPS405, respectively) with optical shutters were combined using a cube polarizer onto a common optical axis. For polarized measurements of $PC_{70}BM$ samples, a 633 nm HeNe laser was used alone. The polarization was rotated using a liquid crystal variable retarder (Meadowlark) and 1/4 wave plate (Thorlabs FR600QM), giving a polarization purity better than 20:1. The polarization and/or wavelength are changed at the end of each trace in the $+x$ direction, allowing time during the retrace for shutters and LC retarder to stabilize. All pd-pcAFM scans have an original resolution of 512 × 512 px. After deinterleaving, the resolution of the four individual photocurrent maps is 512 × 128 px. The estimated incident power density for all illumination sources was ~5 W cm^{-2}.

Conflict of Interest: The authors declare no competing financial interest.

Supporting Information Available: Density functional theory calculations, additional pd-pcAFM data, dark-field TEM data, and an estimation of exponential absorption through the film thickness are supplied in the Supporting Information. This material is available free of charge *via* the Internet at http://pubs.acs.org.

Acknowledgment. S.D.C. and the pd-pcAFM studies were supported by the Institute for Collaborative Biotechnologies through grant W911NF-09-0001 from the U.S. Army Research Office. Supplementary funding for the TEM studies and support for C.J.T. were obtained from the National Science Foundation (DMR-0856060). J.A.L. was supported by the Center for Energy Efficient Materials, an Energy Frontier Research Center funded by the Office of Basic Energy Sciences of the U.S. Department of Energy. We also acknowledge support from the UCSB Center for Scientific Computing NSF CNS-0960316 and the Materials Research Laboratory, an NSF MRSEC (DMR-1121053), for the microscopy facility. C.J.T. would like to acknowledge Michael L. Chabinyc, Edward J. Kramer, Loren G. Kaake, Louis A. Perez, Jacek J. Jasieniak, Greg Welch, Stephan Krämer, Bob Buckley, and Andrew Yeats for helpful discussions and the Peter J. Frenkel Foundation and the National Science Foundation (DMR-0856060) for financial support.

REFERENCES AND NOTES

1. You, J.; Dou, L.; Yoshimura, K.; Kato, T.; Ohya, K.; Moriarty, T.; Emery, K.; Chen, C.-C.; Gao, J.; Li, G.; *et al.* A Polymer Tandem Solar Cell with 10.6% Power Conversion Efficiency. *Nat. Commun.* **2013**, *4*, 1446.
2. Hoppe, H.; Sariciftci, N. S. Morphology of Polymer/Fullerene Bulk Heterojunction Solar Cells. *J. Mater. Chem.* **2006**, *16*, 45–61.
3. Sun, Y.; Welch, G. C.; Leong, W. L.; Takacs, C. J.; Bazan, G. C.; Heeger, A. J. Solution-Processed Small-Molecule Solar Cells with 6.7% Efficiency. *Nat. Mater.* **2012**, *11*, 44–48.
4. van der Poll, T. S.; Love, J. A.; Nguyen, T.-Q.; Bazan, G. C. Non-Basic High-Performance Molecules for Solution-Processed Organic Solar Cells. *Adv. Mater.* **2012**, *24*, 3646–3649.
5. Wei, G.; Xiao, X.; Wang, S.; Sun, K.; Bergemann, K. J.; Thompson, M. E.; Forrest, S. R. Functionalized Squaraine

Donors for Nanocrystalline Organic Photovoltaics. *ACS Nano* **2011**, *6*, 972–978.
6. Walker, B.; Tamayo, A. B.; Dang, X.-D.; Zalar, P.; Seo, J. H.; Garcia, A.; Tantiwiwat, M.; Nguyen, T.-Q. Nanoscale Phase Separation and High Photovoltaic Efficiency in Solution-Processed, Small-Molecule Bulk Heterojunction Solar Cells. *Adv. Funct. Mater.* **2009**, *19*, 3063–3069.
7. Bürckstümmer, H.; Tulyakova, E. V.; Deppisch, M.; Lenze, M. R.; Kronenberg, N. M.; Gsänger, M.; Stolte, M.; Meerholz, K.; Würthner, F. Efficient Solution-Processed Bulk Heterojunction Solar Cells by Antiparallel Supramolecular Arrangement of Dipolar Donor−Acceptor Dyes. *Angew. Chem.* **2011**, *123*, 11832–11836.
8. Lee, O. P.; Yiu, A. T.; Beaujuge, P. M.; Woo, C. H.; Holcombe, T. W.; Millstone, J. E.; Douglas, J. D.; Chen, M. S.; Fréchet, J. M. J. Efficient Small Molecule Bulk Heterojunction Solar Cells with High Fill Factors *via* Pyrene-Directed Molecular Self-Assembly. *Adv. Mater.* **2011**, *23*, 5359–5363.
9. Li, W.; Kelchtermans, M.; Wienk, M. M.; Janssen, R. A. J. Effect of Structure on the Solubility and Photovoltaic Properties of Bis-Diketopyrrolopyrrole Molecules. *J. Mater. Chem. A* **2013**, *1*, 15150–15157.
10. He, G.; Li, Z.; Wan, X.; Zhou, J.; Long, G.; Zhang, S.; Zhang, M.; Chen, Y. Efficient Small Molecule Bulk Heterojunction Solar Cells with High Fill Factors *via* Introduction of [Small Pi]-Stacking Moieties as End Group. *J. Mater. Chem. A* **2013**, *1*, 1801–1809.
11. Liu, Y.; Chen, C.-C.; Hong, Z.; Gao, J.; Yang, Y.; Zhou, H.; Dou, L.; Li, G. Solution-Processed Small-Molecule Solar Cells: Breaking the 10% Power Conversion Efficiency. *Sci. Rep.* **2013**, 3.
12. Lin, Y.; Li, Y.; Zhan, X. Small Molecule Semiconductors for High-Efficiency Organic Photovoltaics. *Chem. Soc. Rev.* **2012**, *41*, 4245–4272.
13. Takacs, C. J.; Sun, Y.; Welch, G. C.; Perez, L. A.; Liu, X.; Wen, W.; Bazan, G. C.; Heeger, A. J. Solar Cell Efficiency, Self-Assembly, and Dipole−Dipole Interactions of Isomorphic Narrow-Band-Gap Molecules. *J. Am. Chem. Soc.* **2012**, *134*, 16597–16606.
14. Jasieniak, J. J.; Hsu, B. B. Y.; Takacs, C. J.; Welch, G. C.; Bazan, G. C.; Moses, D.; Heeger, A. J. Insights into π-Conjugated Small Molecule Neat Films and Blends as Determined through Photoconductivity. *ACS Nano* **2012**, *6*, 8735–8745.
15. Coffey, D. C.; Reid, O. G.; Rodovsky, D. B.; Bartholomew, G. P.; Ginger, D. S. Mapping Local Photocurrents in Polymer/Fullerene Solar Cells with Photoconductive Atomic Force Microscopy. *Nano Lett.* **2007**, *7*, 738–744.
16. Dang, X.-D.; Tamayo, A. B.; Seo, J.; Hoven, C. V.; Walker, B.; Nguyen, T.-Q. Nanostructure and Optoelectronic Characterization of Small Molecule Bulk Heterojunction Solar Cells by Photoconductive Atomic Force Microscopy. *Adv. Funct. Mater.* **2010**, *20*, 3314–3321.
17. Groves, C.; Reid, O. G.; Ginger, D. S. Heterogeneity in Polymer Solar Cells: Local Morphology and Performance in Organic Photovoltaics Studied with Scanning Probe Microscopy. *Acc. Chem. Res.* **2010**, *43*, 612–620.
18. Guide, M.; Dang, X.-D.; Nguyen, T.-Q. Nanoscale Characterization of Tetrabenzoporphyrin and Fullerene-Based Solar Cells by Photoconductive Atomic Force Microscopy. *Adv. Mater.* **2011**, *23*, 2313–2319.
19. Kamkar, D. A.; Wang, M.; Wudl, F.; Nguyen, T.-Q. Single Nanowire OPV Properties of a Fullerene-Capped P3ht Dyad Investigated Using Conductive and Photoconductive AFM. *ACS Nano* **2012**, *6*, 1149–1157.
20. Zhugayevych, A.; Postupna, O.; Bakus, R. C., II; Welch, G. C.; Bazan, G. C.; Tretiak, S. Ab Initio Study of a Molecular Crystal for Photovoltaics: Light Absorption, Exciton and Charge Carrier Transport. *J. Phys. Chem. C* **2013**, *117*, 4920–4930.
21. Eisenmenger, N. D.; Su, G. M.; Welch, G. C.; Takacs, C. J.; Bazan, G. C.; Kramer, E. J.; Chabinyc, M. L. Effect of Bridging Atom Identity on the Morphological Behavior of Solution-Processed Small Molecule Bulk Heterojunction Photovoltaics. *Chem. Mater.* **2013**, *25*, 1688–1698.
22. Lovinger, A. J.; Katz, H. E.; Dodabalapur, A. Direct Imaging of Conducting and Insulating Submolecularly Wide Pathways in an Organic Semiconductor. *Chem. Mater.* **1998**, *10*, 3275–3277.
23. Voigt-Martin, I.; Garbella, R.; Schumacher, M. Structure and Defects in Discotic Crystals and Liquid Crystals as Revealed by Electron Diffraction and High-Resolution Electron Microscopy. *Macromolecules* **1992**, *25*, 961–971.
24. Martin, D. C.; Chen, J.; Yang, J.; Drummy, L. F.; Kübel, C. High Resolution Electron Microscopy of Ordered Polymers and Organic Molecular Crystals: Recent Developments and Future Possibilities. *J. Polym. Sci., Part B: Polym. Phys.* **2005**, *43*, 1749–1778.
25. Brinkmann, M.; Rannou, P. Molecular Weight Dependence of Chain Packing and Semicrystalline Structure in Oriented Films of Regioregular Poly(3-Hexylthiophene) Revealed by High-Resolution Transmission Electron Microscopy. *Macromolecules* **2009**, *42*, 1125–1130.
26. Zhang, X.; Hudson, S. D.; DeLongchamp, D. M.; Gundlach, D. J.; Heeney, M.; McCulloch, I. In-Plane Liquid Crystalline Texture of High-Performance Thienothiophene Copolymer Thin Films. *Adv. Funct. Mater.* **2010**, *20*, 4098–4106.
27. Love, J. A.; Proctor, C. M.; Liu, J.; Takacs, C. J.; Sharenko, A.; van der Poll, T. S.; Heeger, A. J.; Bazan, G. C.; Nguyen, T.-Q. Film Morphology of High Efficiency Solution-Processed Small-Molecule Solar Cells. *Adv. Funct. Mater.* **2013**, *23*, 5019–5026.
28. Thompson, B. C.; Fréchet, J. M. J. Polymer−Fullerene Composite Solar Cells. *Angew. Chem., Int. Ed.* **2008**, *47*, 58–77.
29. O'Connor, B.; Kline, R. J.; Conrad, B. R.; Richter, L. J.; Gundlach, D.; Toney, M. F.; DeLongchamp, D. M. Anisotropic Structure and Charge Transport in Highly Strain-Aligned Regioregular Poly(3-Hexylthiophene). *Adv. Funct. Mater.* **2011**, *21*, 3697–3705.
30. Kyaw, A. K. K.; Wang, D. H.; Gupta, V.; Leong, W. L.; Ke, L.; Bazan, G. C.; Heeger, A. J. Intensity Dependence of Current−Voltage Characteristics and Recombination in High-Efficiency Solution-Processed Small-Molecule Solar Cells. *ACS Nano* **2013**, *7*, 4569–4577.
31. Perez, L. A.; Chou, K. W.; Love, J. A.; van der Poll, T. S.; Smilgies, D. M.; Nguyen, T. Q.; Kramer, E. J.; Amassian, A.; Bazan, G. C. Solvent Additive Effects on Small Molecule Crystallization in Bulk Heterojunction Solar Cells Probed during Spin Casting. *Adv. Mater.* **2013**, *25*, 6380–6384.
32. Collins, B. A.; Cochran, J. E.; Yan, H.; Gann, E.; Hub, C.; Fink, R.; Wang, C.; Schuettfort, T.; McNeill, C. R.; Chabinyc, M. L.; *et al.* Polarized X-Ray Scattering Reveals Non-Crystalline Orientational Ordering in Organic Films. *Nat. Mater.* **2012**, *11*, 536–543.
33. McNeill, C. R.; Ade, H. Soft X-Ray Characterisation of Organic Semiconductor Films. *J. Mater. Chem. C* **2013**, *1*, 187–201.
34. Takacs, C. J.; Treat, N. D.; Krämer, S.; Chen, Z.; Facchetti, A.; Chabinyc, M. L.; Heeger, A. J. Remarkable Order of a High-Performance Polymer. *Nano Lett.* **2013**, *13*, 2522–2527.
35. Savoini, M.; Biagioni, P.; Meskers, S. C. J.; Duò, L.; Hecht, B.; Finazzi, M. Spontaneous Formation of Left- and Right-Handed Cholesterically Ordered Domains in an Enantiopure Chiral Polyfluorene Film. *J. Phys. Chem. Lett.* **2011**, *2*, 1359–1362.
36. Zhang, X.; Bronstein, H.; Kronemeijer, A. J.; Smith, J.; Kim, Y.; Kline, R. J.; Richter, L. J.; Anthopoulos, T. D.; Sirringhaus, H.; Song, K.; *et al.* Molecular Origin of High Field-Effect Mobility in an Indacenodithiophene−Benzothiadiazole Copolymer. *Nat. Commun.* **2013**, 4.
37. Noriega, R.; Rivnay, J.; Vandewal, K.; Koch, F. P. V.; Stingelin, N.; Smith, P.; Toney, M. F.; Salleo, A. A General Relationship between Disorder, Aggregation and Charge Transport in Conjugated Polymers. *Nat. Mater.* **2013**, *12*, 1037–1043.
38. Street, R. A. Unraveling Charge Transport in Conjugated Polymers. *Science* **2013**, *341*, 1072–1073.
39. Headrick, R. L.; Wo, S.; Sansoz, F.; Anthony, J. E. Anisotropic Mobility in Large Grain Size Solution Processed Organic Semiconductor Thin Films. *Appl. Phys. Lett.* **2008**, *92*, 063302.

40. Kim, B.-G.; Jeong, E. J.; Chung, J. W.; Seo, S.; Koo, B.; Kim, J. A Molecular Design Principle of Lyotropic Liquid-Crystalline Conjugated Polymers with Directed Alignment Capability for Plastic Electronics. *Nat. Mater.* **2013**, *12*, 659–664.
41. Diao, Y.; Tee, B. C. K.; Giri, G.; Xu, J.; Kim, D. H.; Becerril, H. A.; Stoltenberg, R. M.; Lee, T. H.; Xue, G.; Mannsfeld, S. C. B.; *et al*. Solution Coating of Large-Area Organic Semiconductor Thin Films with Aligned Single-Crystalline Domains. *Nat. Mater.* **2013**, *12*, 665–671.
42. Darling, S. B. Block Copolymers for Photovoltaics. *Energy Environ. Sci.* **2009**, *2*, 1266–1273.
43. Ku, S.-Y.; Brady, M. A.; Treat, N. D.; Cochran, J. E.; Robb, M. J.; Kramer, E. J.; Chabinyc, M. L.; Hawker, C. J. A Modular Strategy for Fully Conjugated Donor–Acceptor Block Copolymers. *J. Am. Chem. Soc.* **2012**, *134*, 16040–16046.
44. Johnson, K.; Huang, Y.-S.; Huettner, S.; Sommer, M.; Brinkmann, M.; Mulherin, R.; Niedzialek, D.; Beljonne, D.; Clark, J.; Huck, W. T. S.; *et al*. Control of Intrachain Charge Transfer in Model Systems for Block Copolymer Photovoltaic Materials. *J. Am. Chem. Soc.* **2013**, *135*, 5074–5083.
45. Guo, C.; Lin, Y.-H.; Witman, M. D.; Smith, K. A.; Wang, C.; Hexemer, A.; Strzalka, J.; Gomez, E. D.; Verduzco, R. Conjugated Block Copolymer Photovoltaics with near 3% Efficiency through Microphase Separation. *Nano Lett.* **2013**, *13*, 2957–2963.
46. McCulloch, I.; Heeney, M.; Bailey, C.; Genevicius, K.; MacDonald, I.; Shkunov, M.; Sparrowe, D.; Tierney, S.; Wagner, R.; Zhang, W.; *et al*. Liquid-Crystalline Semiconducting Polymers with High Charge-Carrier Mobility. *Nat. Mater.* **2006**, *5*, 328–333.
47. Luria, J. L.; Hoepker, N.; Bruce, R.; Jacobs, A. R.; Groves, C.; Marohn, J. A. Spectroscopic Imaging of Photopotentials and Photoinduced Potential Fluctuations in a Bulk Heterojunction Solar Cell Film. *ACS Nano* **2012**, *6*, 9392–9401.
48. Smieska, L. M.; Pozdin, V. A.; Luria, J. L.; Hennig, R. G.; Hines, M. A.; Lewis, C. A.; Marohn, J. A. Following Chemical Charge Trapping in Pentacene Thin Films by Selective Impurity Doping and Wavelength-Resolved Electric Force Microscopy. *Adv. Funct. Mater.* **2012**, *22*, 5096–5106.
49. Reid, O. G.; Rayermann, G. E.; Coffey, D. C.; Ginger, D. S. Imaging Local Trap Formation in Conjugated Polymer Solar Cells: A Comparison of Time-Resolved Electrostatic Force Microscopy and Scanning Kelvin Probe Imaging. *J. Phys. Chem. C* **2010**, *114*, 20672–20677.
50. Chiesa, M.; Bürgi, L.; Kim, J.-S.; Shikler, R.; Friend, R. H.; Sirringhaus, H. Correlation between Surface Photovoltage and Blend Morphology in Polyfluorene-Based Photodiodes. *Nano Lett.* **2005**, *5*, 559–563.
51. Mastronarde, D. N. Automated Electron Microscope Tomography Using Robust Prediction of Specimen Movements. *J. Struct. Biol.* **2005**, *152*, 36–51.